Electronic Supplementary Material (ESI) for Journal of Materials Chemistry A.

Supporting Information

Single Nickel Atom Supported on Hybridized Graphene-Boron Nitride Nanosheet as a Highly Active Bi-functional Electrocatalyst for Hydrogen and Oxygen Evolution Reactions

Shaobin Tang†, Xunhui Zhou†, Tianyong Liu†, Shiyong Zhang†, Tongtong Yang‡, Yi Luo‡, Edward Sharman§, and Jun Jiang*‡

†Key Laboratory of Organo-Pharmaceutical Chemistry of Jiangxi Province, Gannan Normal University, Ganzhou 341000, China

‡Hefei National Laboratory for Physical Sciences at the Microscale, CAS Key Laboratory of Mechanical Behavior and Design of Materials, School of Chemistry and Materials Science, University of Science and Technology of China, Hefei 230026, China

§Department of Neurology, University of California, Irvine, California 92697, USA

Corresponding Author

*Email: jiangj1@ustc.edu.cn

1 Computational Details

First-principles computations were performed using the projector augmented wave method (PAW)[1] as implemented in the Vienna *ab-initio* simulation package (VASP 5.3).[2,3] The generalized gradient approximation in the form of Perdew-Burke-Ernzerhof (PBE)[4] and a cutoff energy of 550 eV for the plane-wave basis were adopted. Atomic structures were optimized with converging tolerance of 0.02 eV/Å for forces on all atoms, and the energy convergence criterion was set to 10^{-5} eV. The DFT-D2 method by Grimme[5] was employed for long-range van der Waals (vdW) interactions. In order to avoid interaction between two periodic units, a vacuum space of at least 15 Å was used. BCN supercells consisting of 72 atoms, corresponding to lattice parameters of 14.76 × 14.76 × 15 Å, were used, and the Brillouin zone was sampled with 3 × 3 × 1 Monkhorst–Pack k-meshes. The climbing image nudged elastic band (CI-NEB) method [6] was applied to determine the diffusion barrier for the anchored transition metal (TM) atoms. To evaluate the thermal stability of the catalysts, ab initio molecular dynamics (AIMD) simulations were performed in the NVT canonical ensemble;[7] two different temperatures of T = 600 and 1000 K were considered, using a time step of 1 fs. Atomic charges were computed based on Bader's charge population analysis.[8,9]

2 Structural Models

Previous experimental studies[10-12] reported the synthesis of BCN in-plane heterostructures. For example, Ajayan, *et al.*[12] reported the preparation of a new form of 2D atomic film consisting of hybridized h-BN and graphene domains, termed h-BNC materials. It was proposed [12] that the BCN materials consist of randomly distributed domains of h-BN and graphene. Recently, by combination of microstructure characterization and DFT calculations, Gong and Ajayan *et al.*[13] proposed that during conversion process of hexagonal graphene to boron nitride, both triangle BN domain and other irregular BN shape could be formed. However, the precise atomic structures of BCN materials are still controversial.

It is well accepted that the hybrid BCN, whose structure is domain-segregated into two different regions, one consisting of a C-rich domain and other with a BNenriched domain, is more stable thermodynamically than other structures. The BCN models, therefore, are constructed by embedding BN clusters into graphene, including separated BN and graphene domains. Primarily rich B—C bonds in the interface between BN and graphene domain were considered.[14] Figure S1 presents several BCN configurations, involving different BN sizes and triangle- and quadrangle-based BN shapes.[13] These BCN configurations are predicted to be favorable energetically relative to their components (see Figure S2).

Previous works [15-18] showed that for structure of TM SACs on carbon support, the TM atom is coordinated by pyridinic N connecting with carbon atoms to form the active centre of TM-N_x-C. Similarly, to anchor a TM atom onto BCN, several sites of monovacancy defects were considered, such as B, C, and N vacancies (see Figure S3). As a result, the active centers of TM-N_x-C or TM-N_x-B are formed. The binding energy calculations show that compared to the N and C vacancies, the single TM atom is anchored preferably on a B vacancy neighboring three N atoms in the form of TM-N_3-B as revealed in previous work (see Figure S4). [19]

3 ΔG for the Hydrogen Evolution Reaction

For HER, catalytic performance was determined by the binding strength of adsorbed hydrogen:

$$H^+ + e^- + * \rightarrow *H, \tag{1}$$

in which the * represents the active site. Based on the computational hydrogen electrode model,[20] the chemical potential (μ) of a proton-electron pair is equal to half that of H_2 at a potential of 0 V:

$$\mu_{H^+} + \mu_{e^-} = \frac{1}{2}\mu_{H_2} \tag{2}$$

The Gibbs free energy change of the adsorbed state (ΔG_H) under electrode potential U = 0 V can be calculated as:

$$\Delta G_H = \Delta E_H - \Delta E_{ZPE(H)} - T\Delta S_H \tag{3}$$

where ΔE_H is the adsorption energy of hydrogen, $\Delta E_{ZPE(H)}$ and ΔS_H are the differences in the zero-point energy and entropy change between the adsorbed hydrogen and 1/2 H_2 (g), respectively, and T is the temperature (298.15 K). Therefore, the Gibbs free energy with all corrections is considered to be: [21]

$$\Delta G_H = \Delta E_H + 0.24 \text{ eV} \qquad (4)$$

4 ΔG for the Oxygen Evolution Reaction

At pH = 0, the OER involves four elementary steps as follows:

$\Delta G1$ H_2O (l) + * → *OH + H^+ + e^-

$\Delta G2$ *OH → *O + H^+ + e^-

$\Delta G3$ *OH + H_2O (l) → *OOH + H^+ + e^-

$\Delta G4$ *OOH → O_2 (g) + H^+ + e^-

where (l) and (g) represent the liquid phase and gas phase, respectively. The binding energy of the adsorbed intermediates (*O, *OH, *OOH) on TM@BCN are calculated with respect to H_2 and H_2O as follows:

$$\Delta E(*O) = E(*O) - E(*) - [E(H_2O) - E(H_2)] \qquad (5)$$

$$\Delta E(*OH) = E(*OH) - E(*) - [E(H_2O) - 0.5E(H_2)] \qquad (6)$$

$$\Delta E(*OOH) = E(*OOH) - E(*) - [2E(H_2O) - 1.5E(H_2)] \qquad (7)$$

where E(*O), E(*OH), E(*OOH), and E(*) are the DFT total energies of surface binding with O, OH, OOH species and clean surface, respectively. E (H_2O) and E (H_2) are energies of H_2O in the liquid phase and H_2 molecules in the gas phase, respectively.

The free energy changes of each step of the OER were calculated as:[22]

$$\Delta G = \Delta E + \Delta E_{ZPE} - T\Delta S + \Delta G_U + \Delta G_{PH}, \qquad (8)$$

where ΔE, ΔE_{ZPE}, ΔG_U, and ΔS are the electronic energy differences for the reaction, the change in zero-point energies, the free energy change related to electrode potential U, and the entropy change, respectively. The zero-point energy and entropy of the adsorbed state were computed from vibrational frequencies by applying normal mode analysis using DFT calculations. [23] T is taken as room temperature (298.15 K). The entropies and vibrational frequencies of the free molecules were taken from the NIST database.[24] $\Delta G_U = -neU$, where U is an applied electrode potential and n is the number of transferred electrons. $\Delta G_{pH} = 2.303\ k_BT\ pH$, with pH = 0 was employed in this work.

The free energy of H_2O in liquid phase was calculated in the gas phase with a pressure of 0.035 bar, which is the equilibrium vapor pressure of H_2O at T = 298.15 K. To avoid well-known errors of DFT in estimating the energy of O_2 in the high-spin ground state,[25] a free energy value of 4.92 eV for O_2 was derived from $2H_2O \rightarrow O_2 + 2H_2$.

Therefore, ΔG_1, ΔG_2, ΔG_3, and ΔG_4 for the four elementary steps of the OER can be taken as:

$$\Delta G_1 = E(*OH)+\frac{1}{2}E(H_2)-E(H_2O)-E(*)+E_{ZPE(*OH)}+\frac{1}{2}E_{ZPE(H_2)}-E_{ZPE(H_2O)}- \\ T\left[S(*OH)+\frac{1}{2}S(H_2)-S(H_2O)\right]=\Delta E(*OH)+0.24 \tag{9}$$

$$\Delta G_2 = E(*O)+\frac{1}{2}E(H_2)-E(*OH)+E_{ZPE(*O)}+\frac{1}{2}E_{ZPE(H_2)}-E_{ZPE(*OH)}- \\ T\left[S(*O)+\frac{1}{2}S(H_2)-S(*OH)\right]=\Delta E(*O)-\Delta E(*OH)-0.28 \tag{10}$$

$$\Delta G_3 = E(*OOH)+\frac{1}{2}E(H_2)-E(H_2O)-E(*O)+E_{ZPE(*OOH)}+\frac{1}{2}E_{ZPE(H_2)} \\ -E_{ZPE(H_2O)}-E_{ZPE(*O)}-T\left[S(*OOH)+\frac{1}{2}S(H_2)-S(H_2O)-S(*O)\right] \\ =\Delta E(*OOH)-\Delta E(*O)+0.35 \tag{11}$$

$$\Delta G_4 = E(O_2)+\frac{1}{2}E(H_2)+E(*)-E(*OOH)+E_{ZPE(O_2)}+\frac{1}{2}E_{ZPE(H_2)}-E_{ZPE(*OOH)}- \\ T\left[S(O_2)+\frac{1}{2}S(H_2)-S(*OOH)\right]=4.65-\Delta E(*OOH) \tag{12}$$

For all ΔGs, ΔE(*O), ΔE(*OH), and ΔE(*OOH) are calculated from equations (6), (7), and (8), respectively. The theoretical overpotential η for OER is determined by the potential limiting step:

$$\eta = \max\left[\Delta G_1, \Delta G_2, \Delta G_3, \Delta G_4\right]/e - 1.23\ \mathrm{V} \tag{13}$$

For previous many works, [15, 16, 26, 27, 28, 29] the theoretical overpotential η for OER and free energy of adsorbed hydrogen ΔG_H for HER exhibit in accordance results with the electrochemical measurements on the catalytic performance. Thus, herein, the overpotential η and the ΔG_{H*} are selected as indicator for evaluating the OER and HER activity, respectively

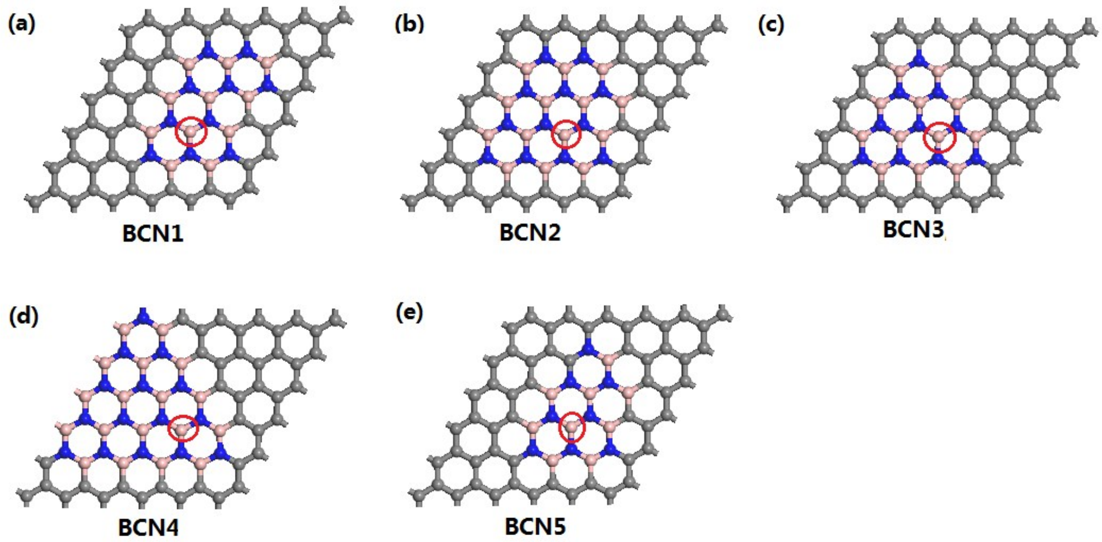

Figure S1. Geometrical structures of the different BCN**n** models (***n*** = 1 to 5). The red circle represents that to anchor TM atom, one boron atom connecting with three N atoms is removed to form a B monovacancy defect B*v* . Such anchored Ni SACs on B*v* is more stable than that on other sites (see Figures S3 and S4).

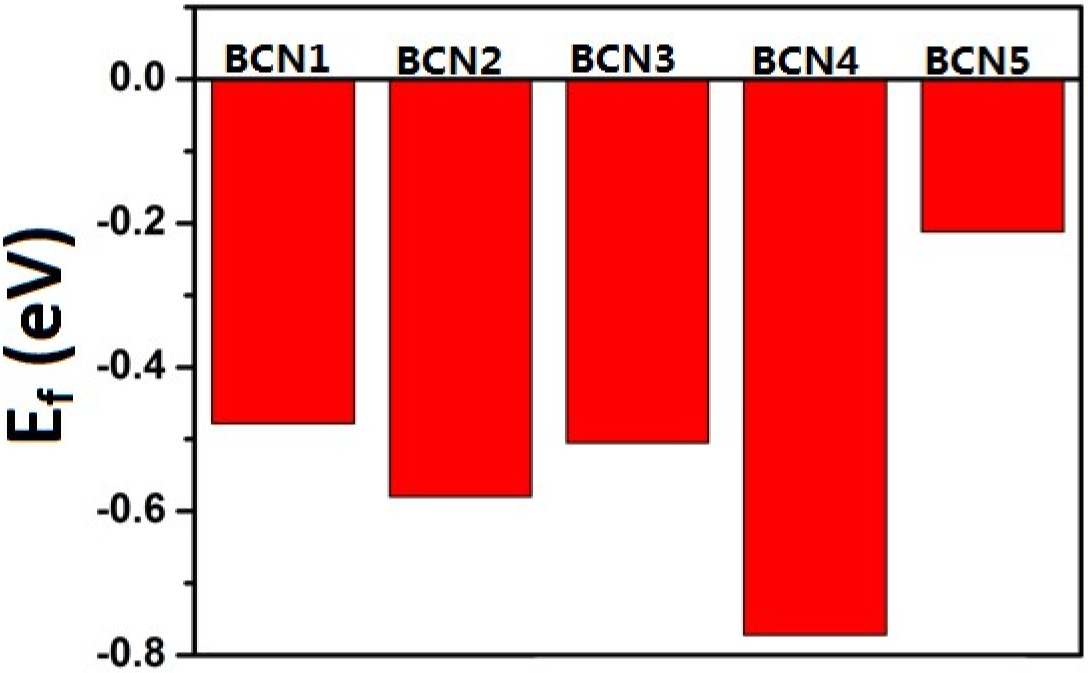

Figure S2. Formation energies of different BCN**n** (***n*** = 1 to 5) configurations relative to their constituents. The corresponding structures are shown in Fig. S1.

To investigate the stability of the hybrid BCN sheet relative to its constituents, a molar formation energy ΔE_f used in binary phase thermodynamics [30,31] can be defined as:

$$\Delta E_f = E(BCN) - \sum_i \chi_i \mu_i \qquad (i = B, C, \text{and } N) \qquad (14)$$

where E(BCN) is the cohesive energy per atom of the BCN heterostructure, χ_i is the molar fraction of atom *i* (*i* = B, C, and N) satisfying $\sum_i \chi_i = 1$, and μ_i is the chemical potential of the constituent *i*. μ_N and μ_C are defined as the binding energies per atom of N_2 and the cohesive energy per atom of a single graphene sheet, respectively. The binding energy per atom of *α*-rhombohedral B is selected as μ_B. The negative ΔE_f (see Figure S2) suggests that the BCN sheet has higher stability than its constituents, indicating the feasibility of their preparation experimentally.

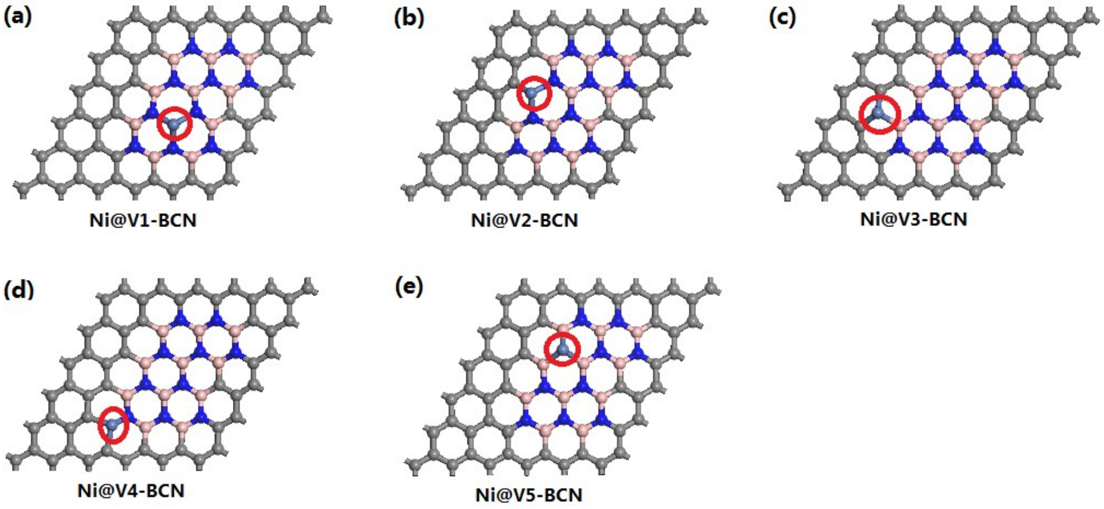

Figure S3. The geometrical structures of Ni supported on various vacancy sites of BCN**1**: boron vacancy with (a) three or (b) two neighboring N atoms, carbon vacancy with one neighboring (c) boron or (d) nitrogen atom, (e) nitrogen vacancy with three neighboring boron atoms. The red circle represents the possible site of Ni atom.

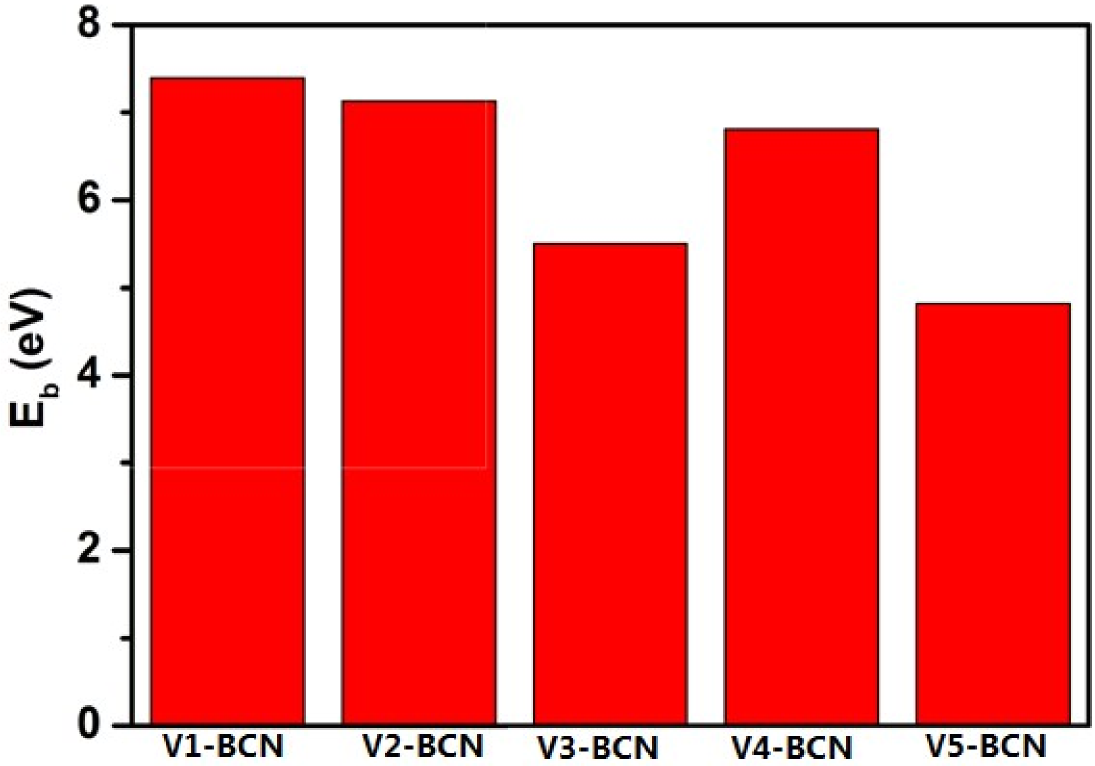

Figure S4. The binding energy of Ni substituted at various vacancy defect sites in the BCN**1** sheet. The corresponding structures are shown in Fig. S3.

Table S1. Calculated binding energies (E_{b} in eV) of TM atoms anchored on BCN**1** with B vacancy site, pyridinic N-doped graphene (N-G), or h-BN with B vacancy site ; cohesive energies (E_{coh} in eV) of TM atoms in the bulk phase; and the energy differences (ΔE_{b} in eV) between them in these two states, are presented.

TM	BCN**1**		N-G		h-BN		Bulk
atoms	E_{b}[1]	$\triangle E_{\mathrm{b}}$	E_{b}	$\triangle E_{\mathrm{b}}$	E_{b}	$\triangle E_{\mathrm{b}}$	E_{coh}[2]
Cr	8.24	3.86	4	-0.38	8.85	4.47	4.38
Mn	7.6	3.87	3.69	-0.04	8.13	4.4	3.73
Fe	8.17	2.6	5.08	-0.49	8.5	2.93	5.57
Co	8.48	2.6	5.44	-0.44	8.82	2.94	5.88
Ni	7.39	2.14	4.71	-0.54	7.73	2.48	5.25
Cu	5.43	1.58	3.36	-0.49	5.78	1.93	3.85
Ag	3.16	0.14	2.07	-0.95	3.45	0.43	3.02
Pd	5.2	0.77	2.69	-1.74	5.54	1.11	4.43
Au	3.29	-1.09	1.66	-2.72	3.76	-0.62	4.38
Pt	6.67	-0.53	3.35	-3.85	7.1	-0.1	7.2
Mo	8.74	1.03	4.63	-3.08	9.34	1.63	7.71

[1] E_{b} is calculated as $E_{\mathrm{b}} = E_{\mathrm{TM}} + E_{\mathrm{S}} - E_{\mathrm{S+TM}}$, where the $E_{\mathrm{S+TM}}$, E_{TM}, and E_{S} are total energies of TM atom-containing substrate, TM atom, and pure substrate, respectively.

[2] E_{coh} is calculated as $E_{\mathrm{coh}} = [\mathrm{n}E_{\mathrm{TM}} - E_{\mathrm{TM(bulk)}}]/\mathrm{n}$, where the E_{TM} and $E_{\mathrm{TM(bulk)}}$ are the energies of TM atoms and their corresponding metal crystal, and n is the number of TM atoms in the crystal.

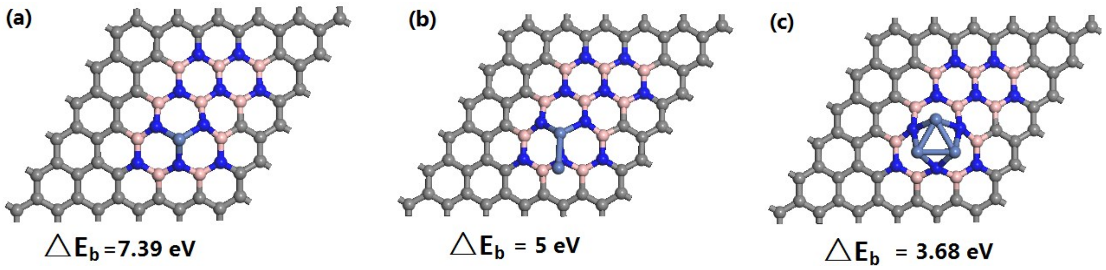

Figure S5. Geometrical structures and corresponding binding energy of (a) one, (b) two, and (c) three Ni atoms on defective BCN1.

To evaluate aggregation of single Ni atoms, we have computed the binding energy for the formation of clusters on BCN**1** sheet with 2 and 3 Ni atoms. As shown in Figure S5, the formation of dispersed single Ni atoms is more favorable energetically than the clusters with 2 and 3 Ni atoms as the corresponding binding energies are 7.39, 5, and 3.68 eV per Ni atom, respectively. The results showed that the aggreation of the TM atom to form clusters is difficult to occur.

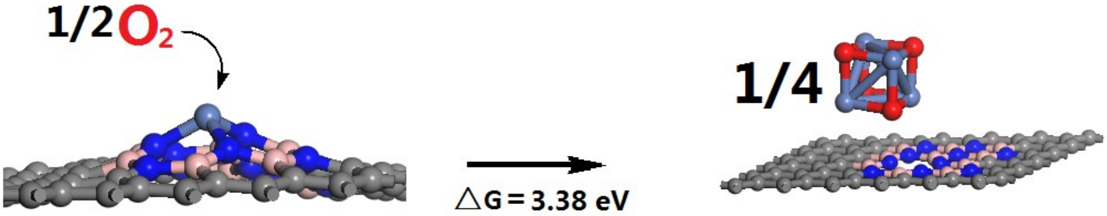

Figure S6. Schematic for Ni oxidation (Ni@BCN + 1/2O_2 (g) = BCN + 1/4 Ni_4O_4 (s)) and corresponding reaction free energy ΔG.

To evalute the oxidation possibility of Ni@BCN**1** during OER, the Gibbs free energy change of Ni oxidation (Ni@BCN**1** + 1/2O_2 (g) = BCN1 + 1/4 Ni_4O_4 (s)) is calculated as shown in Figure S6. The oxidation product of Ni may exist in the form of many kinds of Ni_xO_y, such as NiO and Ni_2O_3. The Ni_2O_3 can be decomposed into NiO and O_2 under 600 ℃. Thus, the Ni_4O_4 cluster from its bulk phase [36] is used as the reference. The ΔG of Ni oxdie formation is calculated as a function of O_2 partial pressure (P_{O_2}) under 298.15 K. The chemical potential of O_2 (μ_{O_2}) was computed based on the equation: $\mu_{O_2} = H^o(T)\text{-}H^o(0) - TS^o(T) + RTIn\left(\frac{p}{p^o}\right)$, where H^o and S^o are the enthalpy and entropy at the pressure $P^o = 1\text{bar}$, respectively. T = 298.15 K was set.

The calculated results showed that the formation Ni_4O_4 cluster is highly endothermic by 3.38 eV, indicating the difficult process. The predicted O_2 patial pressure (P_{O_2}) for formation of Ni_4O_4 cluster under 298.15 K exceeds 10^{58} Pa, suggesting long time stability of Ni SACs under OER operation.

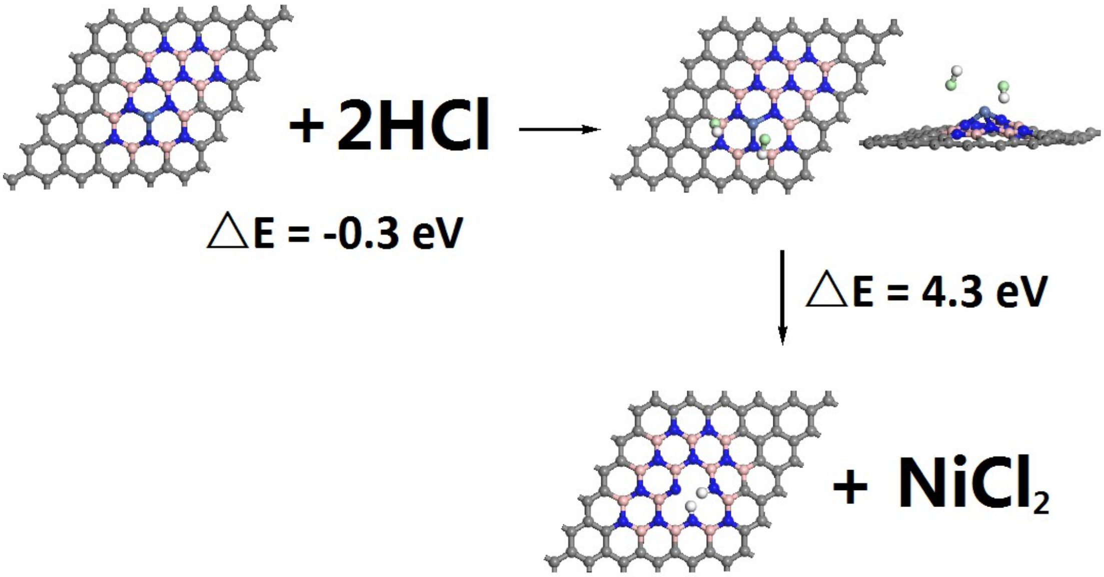

Figure S7. Schematic route for the dissolution process of Ni atom of Ni@BCN**1** in hydrochloric acid (HCl) media and the reaction energy of each step.

We investigate the dissolution possibility of the Ni SACs into the solvent in hydrochloric acid (HCl) media. Figure S7 shows the schematic route for the dissolution process of Ni atom of Ni@BCN**1**. The HCl is first adsorbed on Ni atom with exothermic by 0.3 eV. Subsequently, the Cl atoms in two adsorbed HCl molecules attack the Ni atom until the $NiCl_2$ group is formed, giving rise to one B vacancy. Then, the dissociated H from HCl binds to the N atom around the B vacancy, giving rise to N-H bond. The formation $NiCl_2$ is found to be largely endothermic by 4.3 eV. The calculated results indicate that the dissolution of the Ni SACs into the solvent is unlikely to occur under acid condition, suggesting high stability.

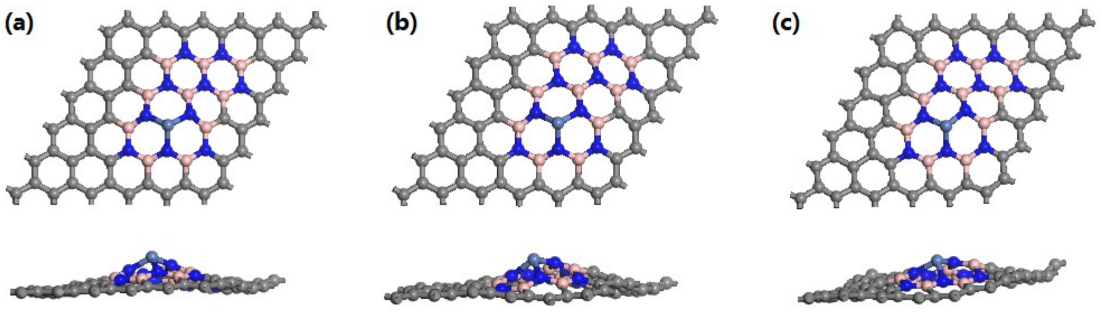

Figure S8. The geometrical structures (top and side view) of Ni@BCN**1** (a) before AIMD simulation and after simulation under (b) T = 600 and (c) 1000 K after 4 ps.

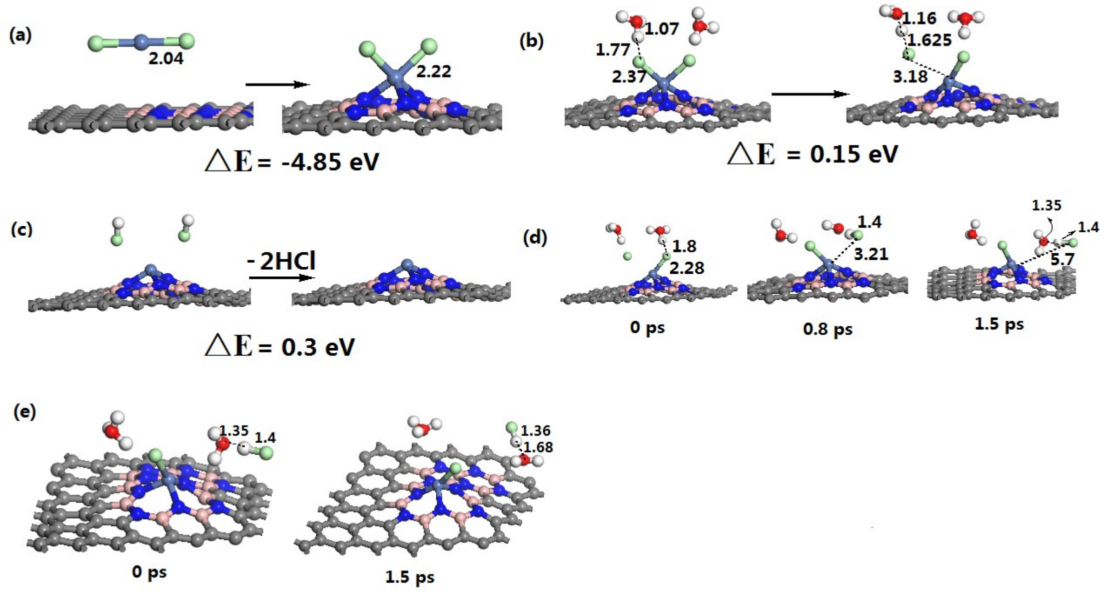

Figure S9. Schematic routes for reaction process: (a) formation of $*NiCl_2$, (b) abstraction of one Cl^- ions by the H^+ from adsorbed H_3O^+, and (c) removel of HCl group from Ni@BCN. (d) The geometrical structures for formation of Ni SACs at MD simulation time of 0, 0.8 and 1.5 ps. (e) similar to that of (d) when using the structure at 1.5 ps in (d) as initial state. The ΔE represent the reaction energy, and all distances are in Å.

For the preparation of TM SACs, the wet chemistry is used to achieve highly dispersed single atom. [32, 33] For such a process, there are two key factors: one is an appropriate precursor, the other is support. To simulate the possibility for synthesis of single Ni anchored on BCN, $NiCl_2$, an important Ni source in industry, was selected as the metal precursor. The formation processes of single Ni atom are given as follows:[33]

$$NiCl_2 + * \rightarrow *NiCl_2$$

$$*NiCl_2 + 2H_3O^+ + 2e^- \rightarrow *Ni(HCl)_2 + 2H_2O$$

$$*Ni(HCl)_2 \rightarrow *Ni + 2HCl$$

Where the * represent the surface of BCN with boron monovacancy.

For the first step, adsorption of a free $NiCl_2$ is largely exothermic by 4.85 eV, indicating a spontaneous process (see Figure S9a). Next, the H^+ from H_3O^+ approaches the Cl^- ions in the adsorbed $NiCl_2$@BCN, forming O-H···Cl bond (Figure S9b). The total energy calculations show that the interaction of H^+ with Cl^- ions is slightly endothermic by 0.19 eV. After formation O-H···Cl bond, the Cl-Ni bond length was increased from 2.37 to 3.18 Å, indicating cleavage of Cl-Ni bond, while the distance H···Cl bond is shortened from 1.77 to 1.62 Å. At last, the HCl groups are easily removed from the catalysts surface, because this group is weakly adsorbed at the Ni site due to a binding energy of -0.3 eV per HCl (Figure S9c). Thus, the single Ni atom anchored on defective BCN could be obtained.

Furthermore, we performed an initio molecular dynamics simulations at the temperature of 350 K as shown in Figure S9d. Clearly, the Cl-Ni bond is gradually broken, and the H-Cl bond is formed after 0.8 ps. When the simulation is further run to 1.5 ps, the Cl^- ions is fully desorbed in the form of HCl groups, leading to the ultimate formation of single Ni atom on BCN sheet.

As shown in Figure S9d, the distance from H in HCl to its neighboring O in H_2O is 1.35 Å. Such small distance shows that there is still a chance to form the H_3O^+, and the Cl^- is re-adsorbed on the Ni atom. To investigate the possibility, the MD simulation was performed using the structure at 1.5 ps (Figure S9d) as initial state. The simulated results (see Figure S9e) shows that the distance between H in HCl and its neighboring O is increased to 1.68 Å from 1.35 Å after 1.5 ps, suggesting low possibility of H_3O^+ recovery.

Table S2. The ΔGs (eV) of the four elementary steps for OER for various TMs in TM@BCN**1**, and the corresponding overpotentials η (V).

TM	ΔG_1	ΔG_2	ΔG_3	ΔG_4	η
Ni	0.35	1.52	1.8	1.29	0.57
Pd	0.26	1.67	1.66	1.37	0.44
Au	0.41	1.52	1.91	1.13	0.68
Cu	0.92	1.92	1.38	0.74	0.69
Fe	-0.35	0.47	2.91	1.93	1.68
Co	0.22	0.7	2.58	1.46	1.35
Cr	-0.88	0.73	2.75	2.36	1.52
Mn	-0.7	0.32	3.12	2.23	1.89
Mo	-1.44	0.2	3.26	2.93	2.03
Pt	-0.35	0.99	2.51	1.81	1.28
Ag	1.09	2.09	1.17	0.61	0.86

Table S3. The ΔGs (eV) of the four elementary steps of the OER for Ni in Ni@BCN**n** (***n*** = 1 to 5), and the corresponding overpotentials η (V).

support	ΔG_1	ΔG_2	ΔG_3	ΔG_4	η
BCN**1**	0.34	1.52	1.8	1.29	0.57
BCN**2**	0.48	1.51	1.7	1.26	0.47
BCN**3**	0.48	1.51	1.72	1.26	0.49
BCN**4**	0.6	1.5	1.71	1.14	0.48
BCN**5**	0.3	1.53	1.78	1.35	0.55

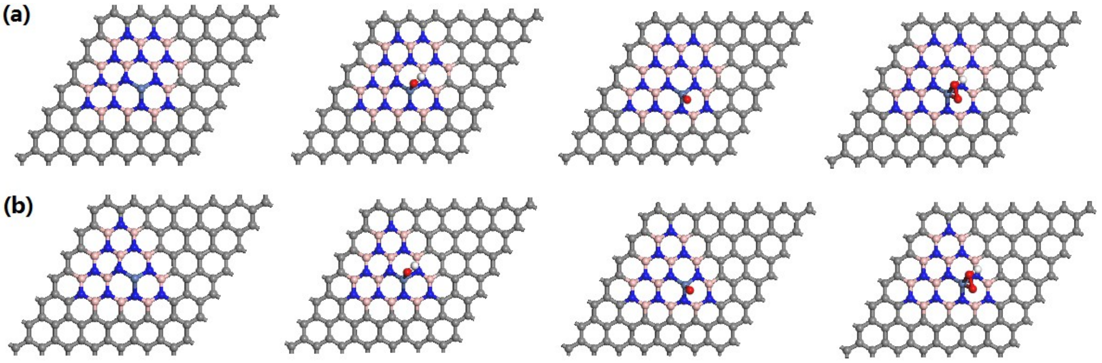

Figure S10. The structures of clean Ni@BCN surface with supercell size consisting of 98 atoms and adsorbed states with *OH, *O, and *OOH species on this surface: (a) BCN**2** and (b) BCN**3.**

Table S4. The binding energy (E_b in eV) of *O, *OH, and *OOH intermediates adsorbed on Ni site on BCN**2** and BCN**3** support with different supercell sizes and corresponding overpotential η for OER (in V). The structures for larger supercell are shown in Figure S.

support	**size (atoms)**	**E_b (*OH)**	**E_b (*O)**	**E_b (*OOH)**	**η**
BCN2	72	0.24	2.02	3.39	0.47
BCN2	98	0.27	2.03	3.4	0.49
BCN3	72	0.24	2.0	3.41	0.49
BCN3	98	0.23	2.01	3.42	0.52

To study the supercell effect, a larger BCN supercells consisting of 98 atoms, corresponding to lattice parameters of 17.22 × 17.22 × 15 Å, were used. The structural models of BCN**2** and BCN**3** support for Ni SACs are only considered. Figure S10 shows the geometrical structures of the adsorbed *OH, *O, and *OOH intermediates. Table S4 summarizes the binding energy of each intermediates on Ni@BCN with different supercell size and the overpotential for OER. Clearly, increasing the supercell size has less influence on the binding strength of intermediate. The calculated overpotential remains nearly unchanged when using the larger BCN supercell.

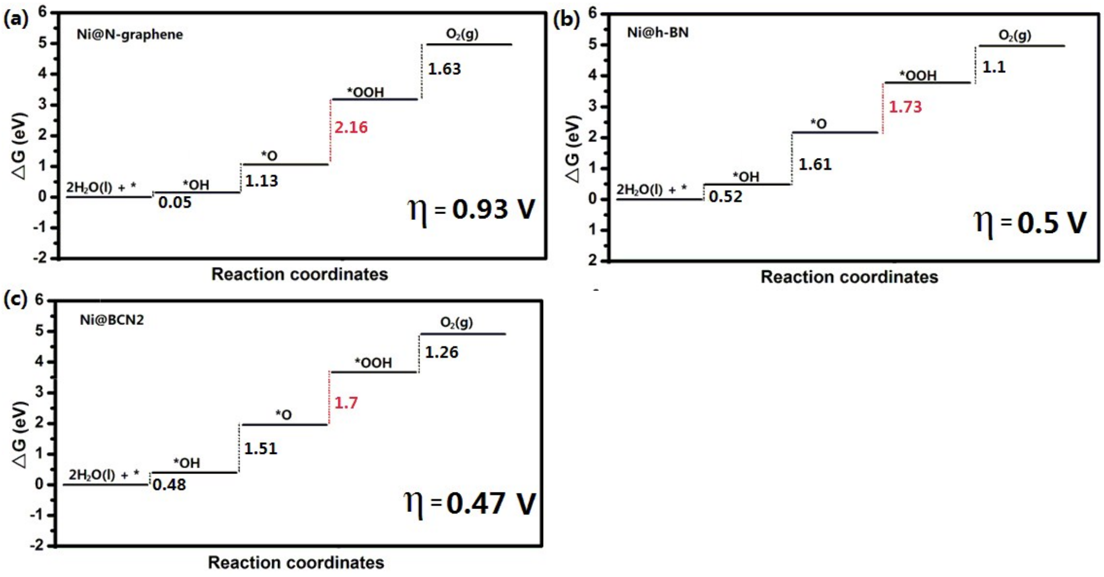

Figure S11. Free energy diagram for OER for Ni in Ni@N-G, h-BN, and BCN**2** at an electrode potential U = 0 V.

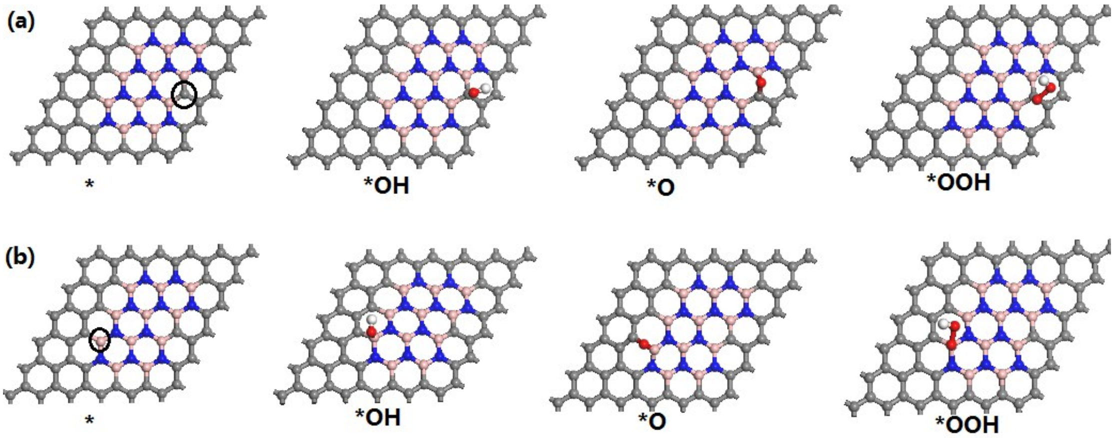

Figure S12. The structures of pure BCN**1** and adsorbed states with *OH, *O, and *OOH species: (a) carbon and (b) boron active sites. The black rings in (a) and (b) represent the C and B active sites, respectively.

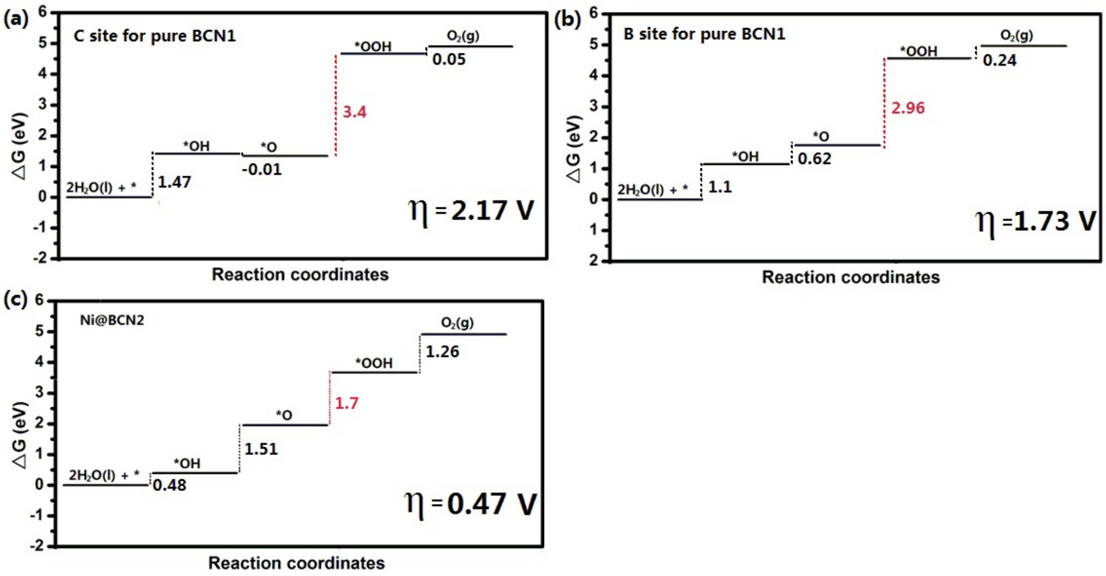

Figure S13. Free energy diagram for OER on (a, b) pure BCN**1** and (c) Ni@BCN**2**. The structures of adsorbed states in (a) and (b) are shown in Fig. S12.

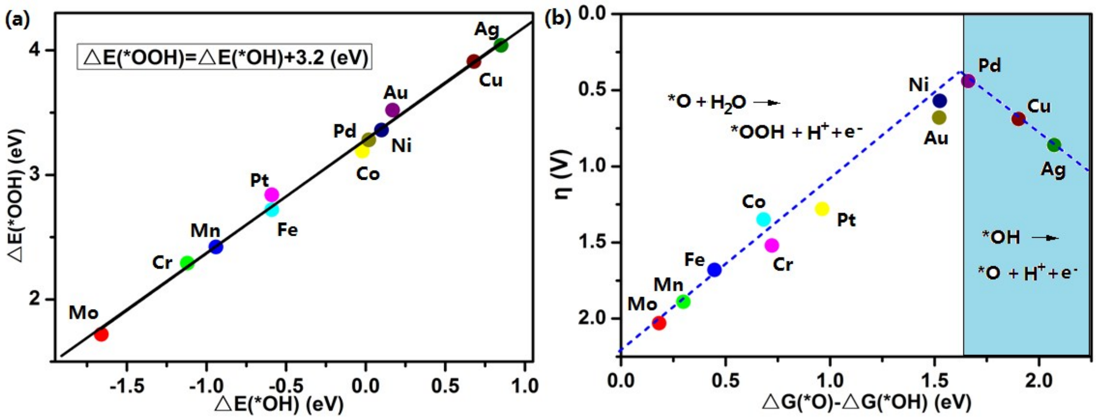

Figure S14. (a) The relationship between *OOH and *OH binding energies and (b) OER overpotential vs free energy difference between *O and *OH species.

By calculating adsorption of *OH and *OOH intermediates on 11 types of TM atom on BCN1, we established the relationship between *OOH and *OH binding energies. As shown in Figure S14a, there is a good scaling relationship between the free energies of *OH and *OOH with a constant slope and an approximate intercept of 3.2 eV. Thus, this constant difference of ΔE(*OOH)-ΔE(*OH) of 3.2 eV is well agreement with that observed on wide range of metal oxides [29] and graphene encapsulating non-precious metals.[28] On the other hand, the slope, which is equal to one, indicates that the *OH and *OOH species have the same bond type on TM atom.

Based on the scaling relationship, the activity of OER can only be determined by the free energy of *O relative to *OH or *OOH, and thus, a single descriptor of ΔG(*O)-ΔG(*OH) was introduced. According to this established descriptor, the theoretical overpotential η exhibits a volcano shape, as shown in Figure S14b. Such universal volcano relationship are also given on many catalyst materials, such as metal oxides [29] and graphene encapsulating non-precious metals.[28] Owing to the linear scaling relationship between the free energies of *OH and *OOH, the unique descriptor for the OER activity is also defined as ΔG(*O)-ΔG(*OOH). Figure 3g shows the similar volcano plot of OER overpotentials.

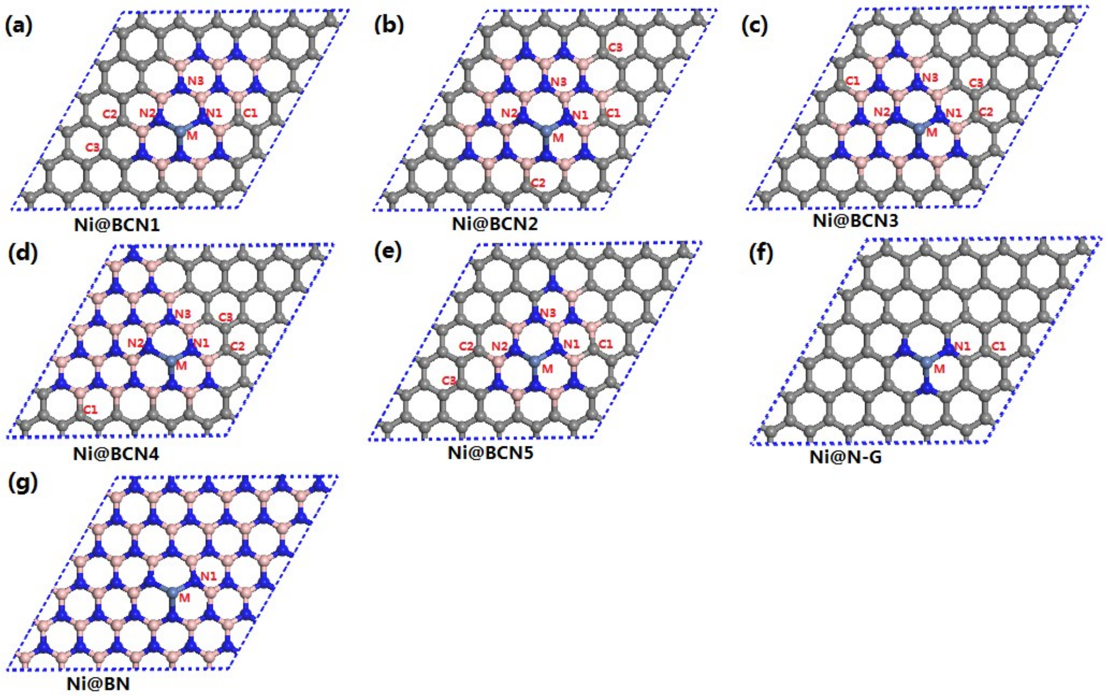

Figure S15. Schematic diagram of various considered sites for HER on Ni@BCN**n** (**n** = 1 to 5), N-G, and BN.

Table S5. The calculated ΔG_H (eV) values for various sites on Ni@BCN**n** (**n** = 1 to 5). The sites are given in Fig. S15.

	M	C1	C2	C3	N1	N2	N3
Ni@BCN**1**	0.36	-0.15	0.27	1.47	-0.04	0.07	0.71
Ni@BCN**2**	0.57	-0.17	0.14	0.61	-0.02	0.08	0.8
Ni@BCN**3**	0.55	0.24	0.37	1.51	0.07	0.2	0.76
Ni@BCN**4**	0.69	0.07	0.26	1.56	0.12	0.28	0.66
Ni@BCN**5**	0.48	-0.09	0.54	0.77	0.15	0.3	1.33

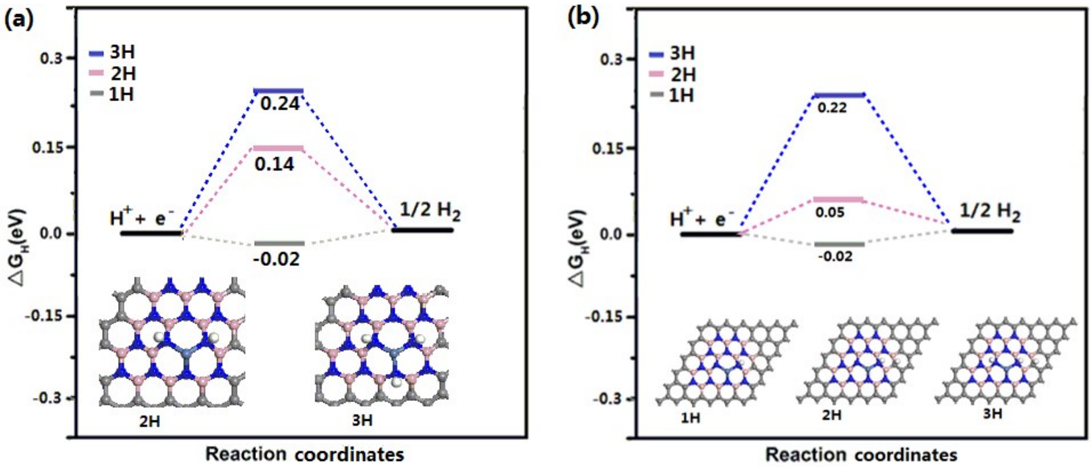

Figure S16. ΔG_H of Ni@BCN**1** with 1, 2, and 3 H adsorptions and the corresponding atomic structures. The second H adsorbed on (a) N atom adjacent to the Ni atom and (b) C atom adjacent to two B.

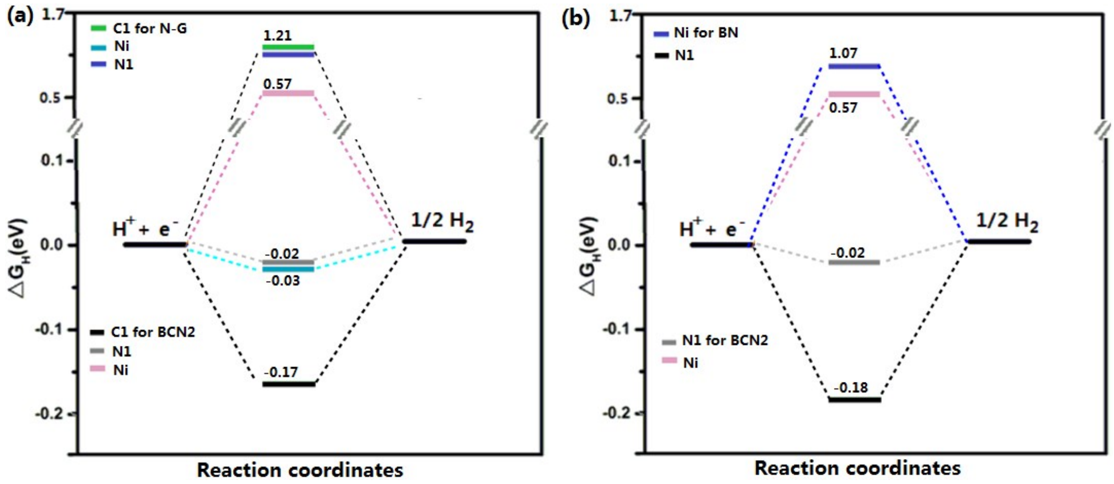

Figure S17. Comparison of ΔG_H values between Ni@BCN**2** and (a) Ni@N-G, and (b) Ni@BN on different sites.

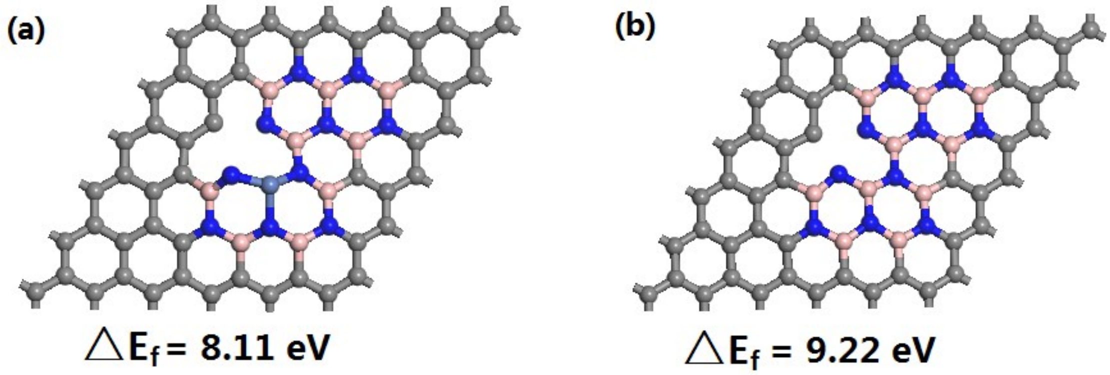

Figure S18. Geometry structure of defective (a) Ni@BCN and pristine BCN with boron vacancy adjacent to the Ni and corresponding formation energy.

Owing to the extensively formed vacancy defects in graphene-based nanomaterials, we also calculated the formation energy of boron vacancy adjacent to N active site on Ni@BCN1 as shown in Figure S18a: $E_f = E_{Ni@BCN1\text{-}v} + E_B - E_{Ni@BCN1}$, where the $E_{Ni@BCN1\text{-}v}$ and $E_{Ni@BCN1}$ are the total energies of Ni@BCN with and without B vacancy. The binding energy per atom of α-rhombohedral B is selected as E_B. The positive E_f indicates the higher stability of systems than the defective one. The total energy calculations showed that forming B vacancy must input an energy of 8.11eV, suggesting the difficult formation of such defect. The B vacancy on Ni@BCN has lower formation energy than the BCN without Ni adsorption (9.22 eV) (Figure S18b).

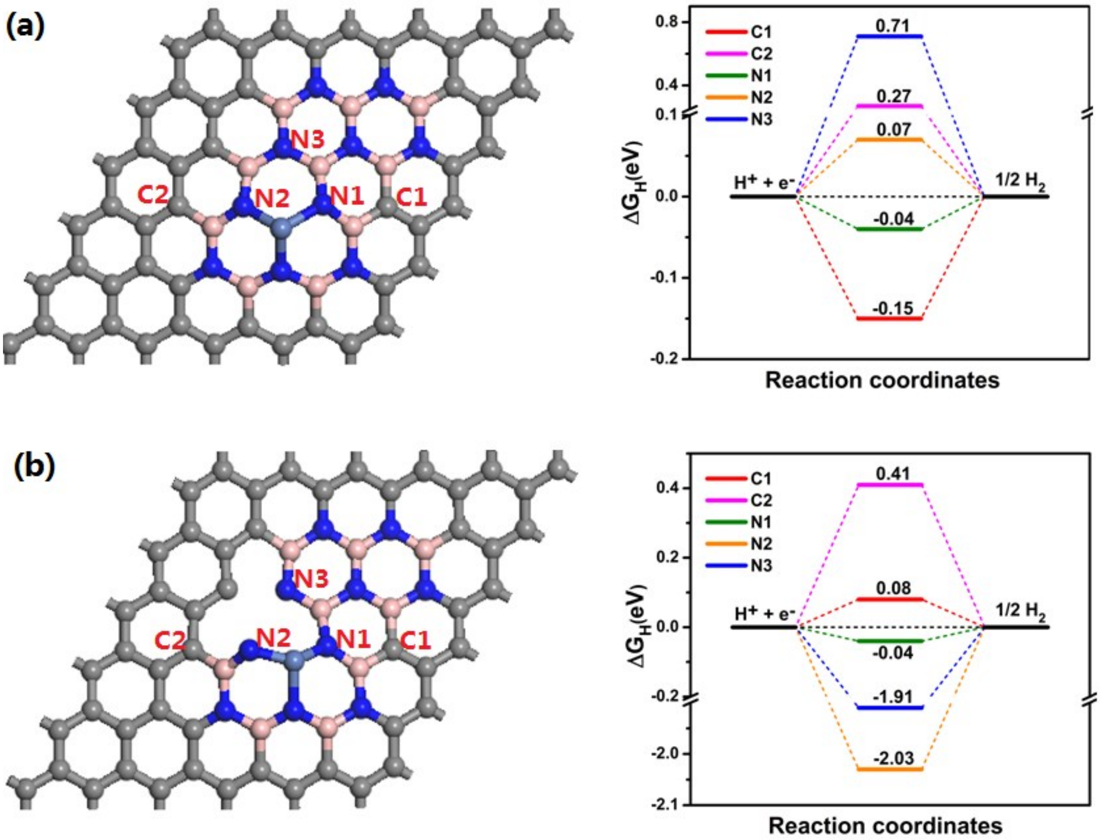

Figure S19. Schematic diagram of various considered sites for HER on Ni@BCN (a) without and (b) with B vacancy defect and corresponding corresponding ΔG_H.

Owing to the preferably formed boron vacancy on h-BN sheet, we discussed effect of such defect on HER performance. As shown in Figure S19, because of introduction of B vacancy, the N atoms in N2 and N3 site around vacancy exhibit large affinity to H atom, with free energy of -2.03 and -1.91 eV, respectively. However, the N1 and C1 sites still remain high HER catalytic activity after formation of B vacancy as the free energies of adsorbed H are -0.04 and 0.08 eV, respectively. Therefore, the Ni@BCN catalysts exhibit high HER activity even in presence of defect.

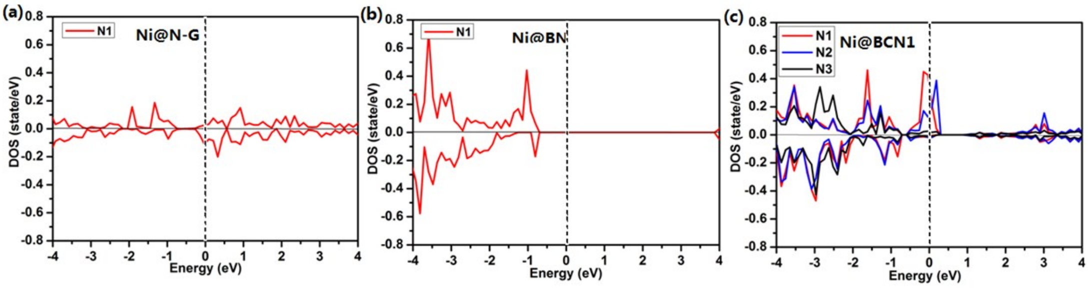

Figure S20. The projected density of states (PDOS) of N atoms on (a) Ni@N-G, (b) Ni@BN, and (c) Ni@BCN**1**. The N1-N3 sites in (c) are shown in Fig. S15a. The Fermi level is set to 0.

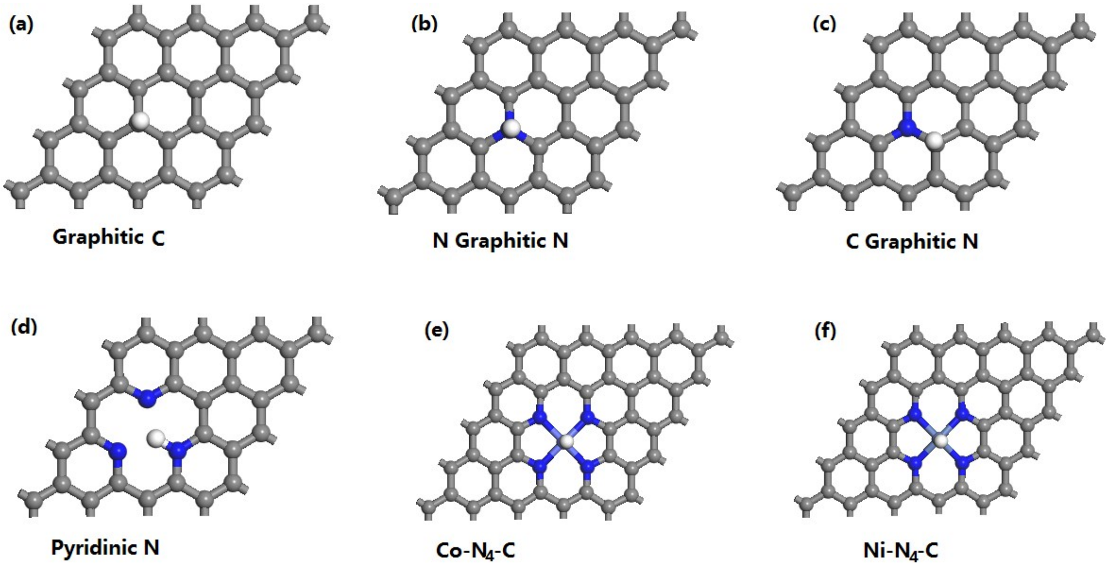

Figure S21. The different graphene-related structural models with H adsorption.

Table S6. Comparison of ΔG_H (in eV) of present method and previous work on different structural models. The active sites with adsorbed H are shown in Fig. S21.

Structural model	present method	previous works
graphitic C	1.54	1.69 (Ref. 16); 1.82 (Ref. 26); 0.79 (Ref. 15)
N graphitic N	1.84	1.89 (Ref. 16)
C graphitic N	0.63	0.89 (Ref. 26); 0.68 (Ref. 27)
Pyridinic N	-2.3	-2.04 (Ref. 26)
Co-N$_4$-C	0.16	0.13 (Ref. 16)
Co-Ni$_4$-C	1.56	1.62 (Ref. 16)

For comparison, we also performed calculations on ΔG_{H*} of selected catalysts from previous works.[15, 16, 26, 27] Figure S21 shows the geometrical structures of theoretical models. Table S6 presents a comparison of this works and previous results for ΔG_{H*}. Clearly, the predicted ΔG_{H*} by this work are consistent with previous results, indicative of the reliability of this methodologies for HER.

Table S7. Comparison of ΔG_H (eV) by PBE and RPBE functional for considered active sites on Ni@BCN. The sites are shown in Figures S13a and b.

structure	**PBE**			**RPBE**		
	C1	N1	N2	C1	N1	N2
Ni@BCN1	-0.15	-0.04	0.07	0.0	0.08	0.19
Ni@BCN2	-0.17	-0.02	0.08	-0.3	-0.18	-0.08

Revised-PBE funcational (RPBE) can describes the binding enrgyies of intermediate with sufficient accuracy.[34] Thus, We performed calculations on ΔG_{H*} of selected sites on Ni@BCN1 and Ni@BCN**2** by RPBE funcational. Table S7 shows a comparison of ΔG_{H*} by PBE and RPBE. The predicted ΔG_{H*} for considered active sites by RPBE still remained the values close to zero, although small difference between the two funcationals is found. Thus, both two funcationals revealed that Ni@BCN materials exhibit high acitvity for HER.

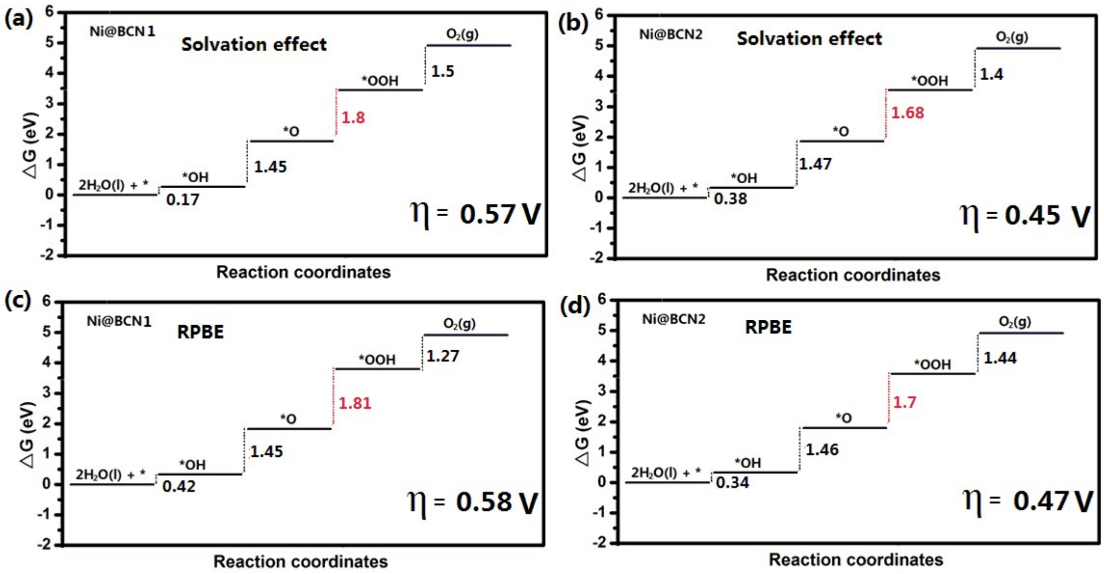

Figure S22. Free energy diagram for OER on Ni@BCN by (a) PBE including solvation effect and (b) RPBE functional at an electrode potential U = 0 V.

For the electrochemical reaction, the solvation may affect on interaction of intermediate with catalyt surface. To investigate the solvent effects, the Poissson-Boltmann implicit solvation model [35] was used. The dielectric constant ε of water is set to 80. We calculated the OER pathway of Ni@BCN1 and Ni@BCN2 with solvation effect using H_2O as solvent, as shown in Fig. S22a and b. Compared to free energy diagram without solvation effect (Figure 3e and f), the predicted overpotential of OER remain less changed as the solvation effect is considered.

To further evaluate the accuracy of our results, we also perfromed the calculations on the OER pathway of Ni@BCN**1** and Ni@BCN**2** by (RPBE). As shown in Figure S22c and d, the RPBE reuslts are consisten with those PBE values (the predicted overpotentials are 0.58 and 0.57 V for Ni@BCN1, respectively).

References

(1) J. P. Perdew, Y. Wang, *Phys. Rev. B* 1992, **45**, 13244.

(2) G. Kresse, J. Furthmüller, *Phys. Rev. B: Condens. Matter Mater. Phys.* 1996, **54**, 11169-11186.

(3) G. Kresse, D. Joubert, *Phys. Rev. B: Condens. Matter Mater. Phys.* 1999, **59**, 1758-1775.

(4) J. P. Perdew, K. Burke, M. Ernzerhof, *Phys. Rev. Lett.* 1996, **77**, 3865.

(5) S. Grimme, *J. Comput. Chem.* 2006, **27**, 1787-1799.

(6) G. Henkelman, B. P. Uberuaga, H. Jonsson, *J. Chem. Phys.* 2000, **113**, 9901-9904.

(7) G. J. Martyna, M. L. Klein, M. Tuckerman, *J. Chem. Phys.* 1992, **97**, 2635-2643.

(8) G. Henkelman, A. Arnaldsson, H. Jónsson, *Comp. Mater. Sci.* 2006, **36**, 354-360.

(9) E. Sanville, S. D. Kenny, R. Smith, G. Henkelman, *J. Comput. Chem.* 2007, **28**, 899-908.

(10) Z. Liu, L. Ma, G. Shi, W. Zhou, Y. Gong, S. Lei, X. Yang, J. Zhang, J. Yu, K. P. Hackenberg, A. Babakhani, J.-C. Idrobo, R. Vajtai, J. Lou, P. M. Ajayan, *Nat. Nanotechnol.* 2013, **8**, 119-124.

(11) L. Liu, J. Park, D. A. Siegel, K. F. McCarty, K. W. Clark, W. Deng, L. Basile, J. C. Idrobo, A. P. Li, G. Gu, *Science.* 2014, **343**, 163-167.

(12) L. Ci, L. Song, C. Jin, D. Jariwala, D. Wu, Y. Li, A. Srivastava, Z. F. Wang, K. Storr, L. Balicas, F. Liu, P. M. Ajayan, *Nat. Mater.* 2010, **9**, 430-435.

(13) Y. Gong, G. Shi, Z. Zhang, W. Zhou, J. Jung, W. Gao, L. Ma, Y. Yang, S. Yang, G. You, R. Vajtai, Q. Xu, A. H. MacDonald, B. I. Yakobson, J. Lou, Z. Liu, P. M. Ajayan, *Nat. Commun.* 2014, **5**, 4193.

(14) M. Chhetri, S. Maitra, H. Chakraborty, U. V. Waghmare, C. N. R. Rao, *Energy Environ. Sci.* 2016, **9**, 95-101.

(15) H. J. Qiu, Y. Ito, W. Cong, Y. Tan, P. Liu, A. Hirata, T. Fujita, Z. Tang, M. Chen, *Angew. Chem. Int. Ed.* 2015, **54**, 14031-14035.

(16) M. D. Hossain, Z. Liu, M. Zhuang, X. Yan, G.-L. Xu, C. A. Gadre, A. Tyagi, I. H. Abidi, C.-J. Sun, H. Wong, A. Guda, Y. Hao, X. Pan, K. Amine, Z. Luo, *Adv. Energy Mater.* 2019, **9**, 1803689.

(17) H.-W. Liang, S. Brüller, R. Dong, J. Zhang, X. Feng, K. Müllen, *Nat. Commun.* 2015, **6**, 7992.

(18) H. Fei, J. Dong, M. J. Arellano-Jimenez, G. K. Ye, N. D., E. L. G. Samuel, Z. Peng, Z. Zhu, F. Qin, J. Bao, M. J. Yacaman, P. M. Ajayan, D. Chen, J. M. Tour, *Nat. Commun.* 2015, **6**, 8668.

(19) J. Zhao, Z. Chen, *J. Am. Chem. Soc.* 2017, **139**, 12480-12487.

(20) J. K. Norskov, J. Rossmeisl, A. Logadottir, L. Lindqvist, J. R. Kitchin, T. Bligaard, H. Jonsson, *J. Phys. Chem. B* 2004, **108**, 17886-17892.

(21) J. Nørskov, T. Bligaard, A. Logadottir, J. Kitchin, J. Chen, S. Pandelov, *J. Electrochem. Soc.* 2005, **152**, J23-J26.

(22) M. Li, L. Zhang, Q. Xu, J. Niu, Z. Xia, *J. Catal.* 2014, **314**, 66-72.

(23) Y.-A. Zhu, D. Chen, X.-G. Zhou, W.-K. Yuan, *Catal. Today.* 2009, **148**, 260-267.

(24) Computational Chemistry Comparison and Benchmark Database. http://cccbdb.nist.gov/.

(25) J. Rossmeisl, Z. W. Qu, H. Zhu, G. J. Kroes, J. K. Nørskov, *J. Electroanal. Chem.* 2007, **607**, 83-89.

(26) J.-S. Li, Y. Wang, C.-H. Liu, S.-L. Li, Y.-G. Wang, L.-Z. Dong, Z.-H. Dai1, Y.-F. Li, Y.-Q. Lan, *Nat. Commun.* 2016. **7***,* 11204.

(27) Y. Ito, W. Cong, T. Fujita, Z. Tang, M. Chen, *Angew. Chem. Int. Ed*. 2015, **54**, 2131-2136.

(28) X.Cui, P. Ren, D. Deng, J. Deng, X. Bao, *Energy Environ. Sci.,* 2016, **9**, 123-129.

(29) I. C. Man, H.-Y. Su, F. Calle-Vallejo, H. A. Hansen, J. I. Martínez, N. G. Inoglu, J. Kitchin, T. F. Jaramillo, J. K. Nørskov, *ChemCatChem.* 2011, **3**, 1159-1165.

(30) E.-j. Kan, Z. Li, J. Yang, J. G. Hou, *J. Am. Chem. Soc.* 2008, **130**, 4224-4225.

(31) V. Barone, O. Hod, G. E. Scuseria, *Nano Lett.* 2006, **6**, 2748-2754.

(32) X.-F. Yang, A. Wang, B. Qiao, J. Li, J. Liu, T. Zhang, *Acc. Chem. Res*. 2013, **46***,* 1740-1748.

(33) B. Qiao, A. Wang, X. Yang, L. F. Allard, Z. Jiang, Y. Cui, J. Liu, Jun. Li, T. Zhang, *Nat. Chem.* 2011, **3**, 634-641.

(34) B. Hammer, L. B. Hansen, J. K. Nørskov, *Phys. Rev. B: Condens. Matter Mater. Phys*., 1999, **59**, 7413-7421.

(35) K. Mathew, R. Sundararaman, K. Letchworth-Weaver, T. Arias, R. G. Hennig, *J. Chem. Phys.* 2014, **140**, 084106.

(36) R. Cairns, E. Ott, *J. Am. Chem. Soc.* 1933, **55**, 527.